

# Soft, Skin-Interfaced Microfluidic Systems with Wireless, Battery-Free Electronics for Digital, Real-Time Tracking of Sweat Loss and Electrolyte Composition

Sung Bong Kim, KunHyuck Lee, Milan S. Raj, Boram Lee, Jonathan T. Reeder, Jahyun Koo, Aurélie Hourlier-Fargette, Amay J. Bandodkar, Sang Min Won, Yurina Sekine, Jungil Choi, Yi Zhang, Jangryeol Yoon, Bong Hoon Kim, Yeojeong Yun, Seojin Lee, Jiho Shin, Jeonghyun Kim, Roozbeh Ghaffari, and John A. Rogers\*

Sweat excretion is a dynamic physiological process that varies with body position, activity level, environmental factors, and health status. Conventional means for measuring the properties of sweat yield accurate results but their requirements for sampling and analytics do not allow for use in the field. Emerging wearable devices offer significant advantages over existing approaches, but each has significant drawbacks associated with bulk and weight, inability to quantify volumetric sweat rate and loss, robustness, and/or inadequate accuracy in biochemical analysis. This paper presents a thin, miniaturized, skin-interfaced microfluidic technology that includes a reusable, battery-free electronics module for measuring sweat conductivity and rate in real-time using wireless power from and data communication to electronic devices with capabilities in near field communications (NFC), including most smartphones. The platform exploits ultrathin electrodes integrated within a collection of microchannels as interfaces to circuits that leverage NFC protocols. The resulting capabilities are complementary to those of previously reported colorimetric strategies. Systematic studies of these combined microfluidic/electronic systems, accurate correlations of measurements performed with them to those of laboratory standard instrumentation, and field tests on human subjects exercising and at rest establish the key operational features and their utility in sweat analytics.

## 1. Introduction

Human sweat regulates body temperature dynamically in response to environmental factors and physiological conditions.<sup>[1–5]</sup> A single droplet of sweat contains a heterogeneous blend of biomarkers, including electrolytes, glucose, lactate, hormones, enzymes, and proteins, each of which can change rapidly in response to exogenous agents (e.g., pharmacological agents or alcohol)<sup>[6,7]</sup> or to cognitive strain, physical fatigue, dehydration, or disease state (e.g., cystic fibrosis).<sup>[8–10]</sup> Diagnostic instruments that rely on sweat samples collected using absorbant pads yield a wealth of information related to physiological status and athletic performance.<sup>[11,12]</sup> The protocols and the benchtop systems required for this purpose are, however, incompatible with real-time monitoring in the field, due to the bulk and expense of the hardware and the time and effort required for sample collection and preparation.

Dr. S. B. Kim, S. M. Won, Dr. J. Yoon, Y. Yun, J. Shin  
Department of Materials Science and Engineering  
University of Illinois at Urbana-Champaign  
Urbana, IL 61801, USA

Dr. S. B. Kim, S. M. Won, Dr. J. Yoon, Dr. B. H. Kim, Y. Yun, S. Lee, J. Shin  
Frederick Seitz Materials Research Laboratory  
University of Illinois at Urbana-Champaign  
Urbana, IL 61801, USA

K. Lee, M. S. Raj, Dr. J. T. Reeder, Dr. J. Koo, Dr. A. Hourlier-Fargette,  
Dr. A. J. Bandodkar, Dr. J. Choi, Dr. Y. Zhang, Dr. B. H. Kim,  
Prof. R. Ghaffari, Prof. J. A. Rogers  
Center for Bio-Integrated Electronics at the Simpson  
Querrey Institute for BioNanotechnology  
Northwestern University  
Evanston, IL 60208, USA  
E-mail: jrogers@northwestern.edu

K. Lee, Dr. J. T. Reeder, Dr. J. Koo, Dr. A. Hourlier-Fargette,  
Dr. A. J. Bandodkar, Dr. J. Choi, Dr. Y. Zhang, Prof. J. A. Rogers  
Department of Materials Science and Engineering  
Northwestern University  
Evanston, IL 60208, USA

Dr. B. Lee  
Department of Medicine  
Konkuk University  
Seoul 05029, South Korea

Dr. Y. Sekine  
Materials Sciences Research Center  
Japan Atomic Energy Agency  
Tokai, Ibaraki 319-1195, Japan

Dr. Y. Zhang  
Department of Biomedical, Biological, and Chemical Engineering  
University of Missouri  
Columbia, MO 65211, USA

 The ORCID identification number(s) for the author(s) of this article can be found under <https://doi.org/10.1002/sml.201802876>.

DOI: 10.1002/sml.201802876

Recent advances in flexible, hybrid electronics, soft microfluidics, and electrochemical sensors serve as foundations for emerging classes of skin-mounted systems for measuring the properties of sweat, each with features that overcome key limitations of conventional technologies.<sup>[13–16]</sup> Other electrochemical measurement systems designed for sweat do not provide measurements of sweat rate or sweat loss, and most rely on power from on-board batteries with significantly larger sizes, thicknesses and weights compared to those reported here. These comparatively large form factors support less robust and comfortable interfaces to the skin.<sup>[13,17]</sup> Furthermore, the hydrogels and/or absorbent materials that typically enable local capture of sweat do not support analysis of sweat rate, total sweat loss, or electrolyte loss, each of which is critically important in managing athletic performance and clinical health. In addition, the rate of sweating affects the concentrations of biomarkers in sweat, in ways that can be calibrated only when the rate is known. Recently reported soft, skin-compatible microfluidic systems offer many of these unique capabilities, but their colorimetric approaches for sensing require careful control and calibration of ambient lighting conditions for accurate readings.<sup>[15,18,19]</sup>

This paper presents a variant of this type of microfluidic system that uses, instead of colorimetrics, integrated electrodes as an electrical interface to a thin, battery-free, wireless electronic module configured for measurement of sweat, in real-time, as it is excreted from the epidermis. Specifically, this platform allows sweat loss, instantaneous sweat rate, and sodium/chloride concentrations to be recorded wirelessly in remote environments via a smartphone or other device with capabilities in near field communications (NFC). Pilot field

studies on healthy subjects demonstrate capabilities for accurate measurements of sweat biomarkers and dynamics in uncontrolled gym and sauna settings, with robust, nonirritating interfaces to the skin.

## 2. Results and Discussion

### 2.1. NFC-Enabled, Soft Microfluidic System for Digital, Wireless Measurements of Sweat Rate, Sweat Loss, and Electrolyte Concentration

Precise measurements of sweat loss, rate, and electrolyte content require advanced classes of soft microfluidic systems that directly interface with the skin. Previously reported designs use networks of microchannels with colored dyes or color responsive chemistries for determining the sweat excretion rate and the total volume of excreted sweat by visual inspection or analysis of digital images at various time-points.<sup>[15]</sup> The approach described here introduces capabilities for direct digital readout via a wireless, radio frequency (RF) battery-free electronic interface to a smartphone, or other NFC-enabled device. An array of electrodes configured along the lengths of the microchannels establishes electrical interfaces directly to excreted sweat for measurements of total resistance in a way that yields quantitative information on sweat rate and loss, and on electrolyte concentration.

The main sub-systems include a soft microfluidic structure with integrated electrodes, a reusable, battery-free NFC electronics module and a skin-safe adhesive layer with openings to the underlying skin to define zones for collecting sweat (**Figure 1a**). As shown in **Figure 1b** and **Figure S1a** in the Supporting Information, this sub-system consists of a gold (Au)-coated collection of copper (Cu) electrodes defined photolithographically and supported by a thin layer of polyimide (PI,  $\approx 1.5 \mu\text{m}$  thickness; **Figure 1b**). The PI includes a bilayer of Ti (100 Å) and SiO<sub>2</sub> (400 Å) on its back surface to facilitate chemical bonding to a planar thin sheet of poly(dimethylsiloxane) (PDMS, Dow Corning; 20:1 mixture of base to curing agent, spin cast on a petri dish) (**Figure 1c**). A separate piece of PDMS, with molded relief structures on its surface, bonds in an aligned fashion to this substrate, to yield an instrumented, soft microfluidic platform with integrated electrodes as interfaces to sweat as it fills the microchannels (**Figure 1d** and **Figure S1b**, Supporting Information).

Separate inlet openings on the skin side of the microfluidic platform lead to two separate microchannel structures. The first serves as a reference and includes a single pair of electrodes with well-defined spacing (6961  $\mu\text{m}$ ) (**Figure 1e** and **Figure S2a**, Supporting Information). When this segment of the microchannel is filled, a measurement of resistance, together with computed volume of sweat captured between the electrodes (0.835  $\mu\text{L}$ ), yields sweat conductivity. By applying a calibration factor to this conductivity estimate, we can determine the concentration of electrolytes (predominantly sodium chloride) in a given sweat sample, as described in the following section.

We apply an AC measurement mode to minimize double-layer charge effects near the electrodes and thereby limit cumulative migration of ions, which tend to mask the

S. Lee

Department of Molecular and Cellular Biology  
University of Illinois at Urbana-Champaign  
Urbana, IL 61801, USA

Prof. J. Kim

Department of Electronics Convergence Engineering  
Kwangwoon University  
Seoul 01897, Republic of Korea

Prof. R. Ghaffari, Prof. J. A. Rogers

Department of Biomedical Engineering  
Northwestern University  
Evanston, IL 60208, USA

Prof. J. A. Rogers

Department of Chemistry  
Northwestern University  
Evanston, IL 60208, USA

Prof. J. A. Rogers

Department of Electrical Engineering and Computer Science  
Northwestern University  
Evanston, IL 60208, USA

Prof. J. A. Rogers

Department of Neurological Surgery  
Northwestern University  
Evanston, IL 60208, USA

Prof. J. A. Rogers

Simpson Querrey Institute for Nano/Biotechnology  
McCormick School of Engineering and Feinberg  
School of Medicine  
Northwestern University  
Evanston, IL 60208, USA

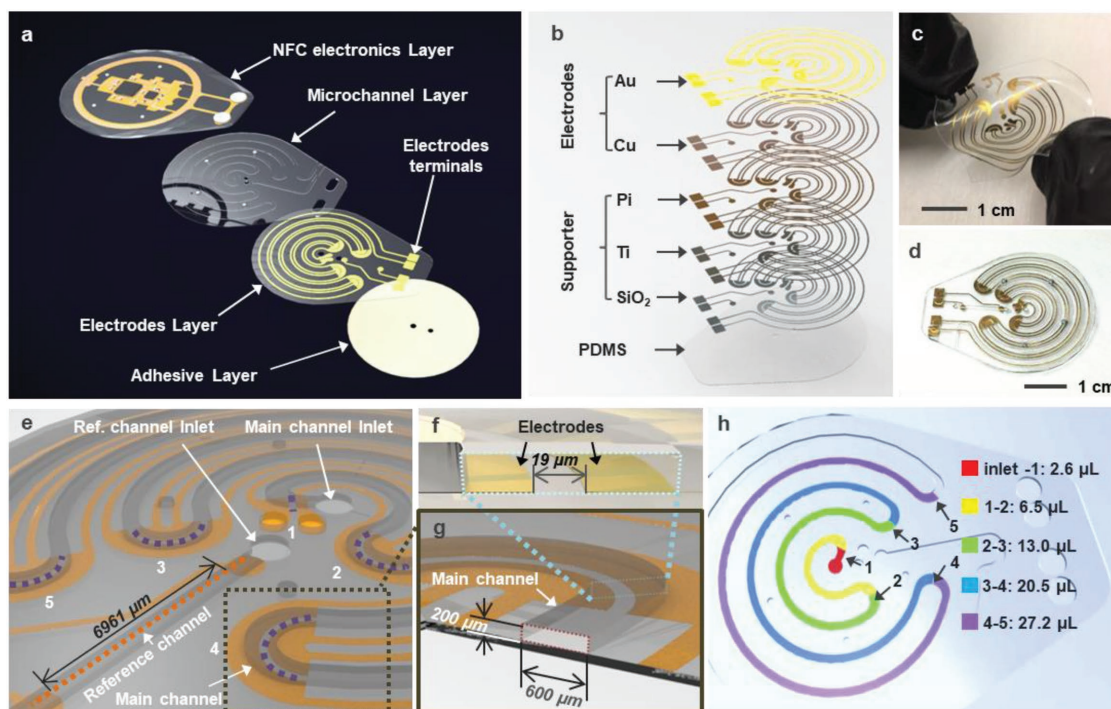


**Figure 1.** Schematic illustrations, pictures, and equivalent circuit diagrams of a battery-free, wireless microfluidics system with capabilities in digital measurements of sweat loss, sweat rate, and electrolyte concentration. a) Exploded illustration of the various layers of a typical device. b) Exploded view schematic illustration of the electrodes layer. c) Optical image of the electrodes layer in a bent configuration. d) Optical image of an assembled microfluidic system with integrated flexible electrodes. e) Magnified illustration of a portion of the system to highlight the main and reference microchannel structures. The purple dotted lines identify the probing pads in the main channel, each designated with a number that defines the temporal order of contact with sweat as it fills the channel. The orange dotted line defines the reference channel. f) Cross-sectional illustration of a microchannel that shows the dimensions of a pair of probing pads. g) Cross-sectional illustration that shows the dimensions of the microchannels. h) Illustration to highlight the volumes of sweat that lie between pairs of probing pads. The different colors highlight the positions of each pair, with volumes for each corresponding segment of microchannel.

electrolyte concentration estimates.<sup>[20–22]</sup> The open outlet of this microchannel allows continuous, uninterrupted flow of sweat driven by the eccrine glands, such that a measurement of conductivity performed at a given instant in time corresponds to the real-time electrolyte concentrations of sweat being excreted from the skin. This design enables measurement of time dependent variations of sweat rate and electrolyte loss.<sup>[3]</sup>

The second microchannel structure represents the part of the microfluidic platform to measure sweat loss. This channel guides the flow of sweat from a separate inlet port, across five pairs of probing pads associated with a single pair of electrode lines, where the pads (labeled as 1, 2, 3, 4, and 5, each with separations of  $\approx 19 \mu\text{m}$ ; Figure 1e,f) lie sequentially along the filling path of channel. The depth of the main channel ( $200 \mu\text{m}$  depth,  $600 \mu\text{m}$  width; Figure 1g) and the separation between the pairs of pads define the measured volumes of sweat, as shown in Figure 1h. The total volume of this channel structure is  $\approx 80 \mu\text{L}$ , which corresponds to the amount of sweat released across the inlet region for moderate rates of sweating from the arm for 20–40 min.

The presence of sweat between pairs of probing pads forms a conductive path for passage of AC current. The digital readout system compares measured resistances to known reference resistors,  $R_a$  and  $R_b$ . An NFC microcontroller (RF430, ISO15693 interface) then generates an AC voltage

( $V_{\text{TMS}} = 1.5 \text{ V}$ ). The terminals of a pair of analog-to-digital converters (ADCs, 16384 unit codes across 0–0.9 V range) read output voltages, as shown in the equivalent circuit diagram (Figure 2a). These voltages, denoted ADC0 and ADC1, are described by the following equations

$$\begin{aligned} \text{ADC0} &= V_{\text{TMS}} \times \frac{R_b}{R_b + R_r} - V_f \\ \text{ADC1} &= V_{\text{TMS}} \times \frac{R_a}{R_a + R_n} - V_f \quad (n = 1, 2, 3, 4, \text{ and } 5) \end{aligned} \quad (1)$$

where  $V_f$  is the forward voltage of the rectifier ( $\approx 150 \text{ mV}$ ),  $R_n$  is the resistance across the pair of electrodes that reside along the main microchannel when it is filled with sweat to a location just beyond the  $n$ th pair of probing pads and  $R_r$  is the resistance across the reference electrodes. Figure 2b presents a schematic illustration of the reference and main electrode pairs and the principle associated with measurements of  $R_n$  and  $R_r$ , with representative values for sweat at typical electrolyte concentrations. As the resistance of the Au/Cu traces can be ignored, the total resistance ( $R_n$ ) depends on the number of pairs of probing pads that are bridged by sweat, the volume of sweat between these pairs, the conductivity of the sweat and the resistance of the relevant lengths of Au/Cu traces. The resulting expression is

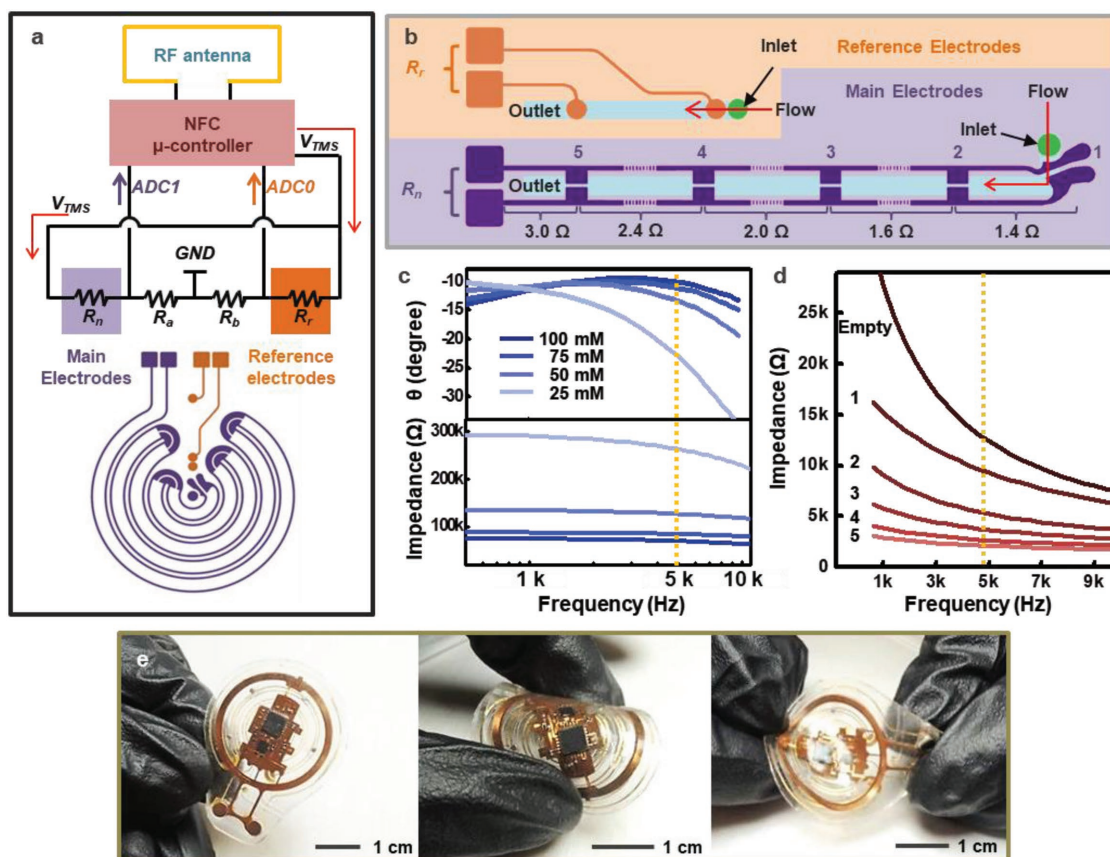


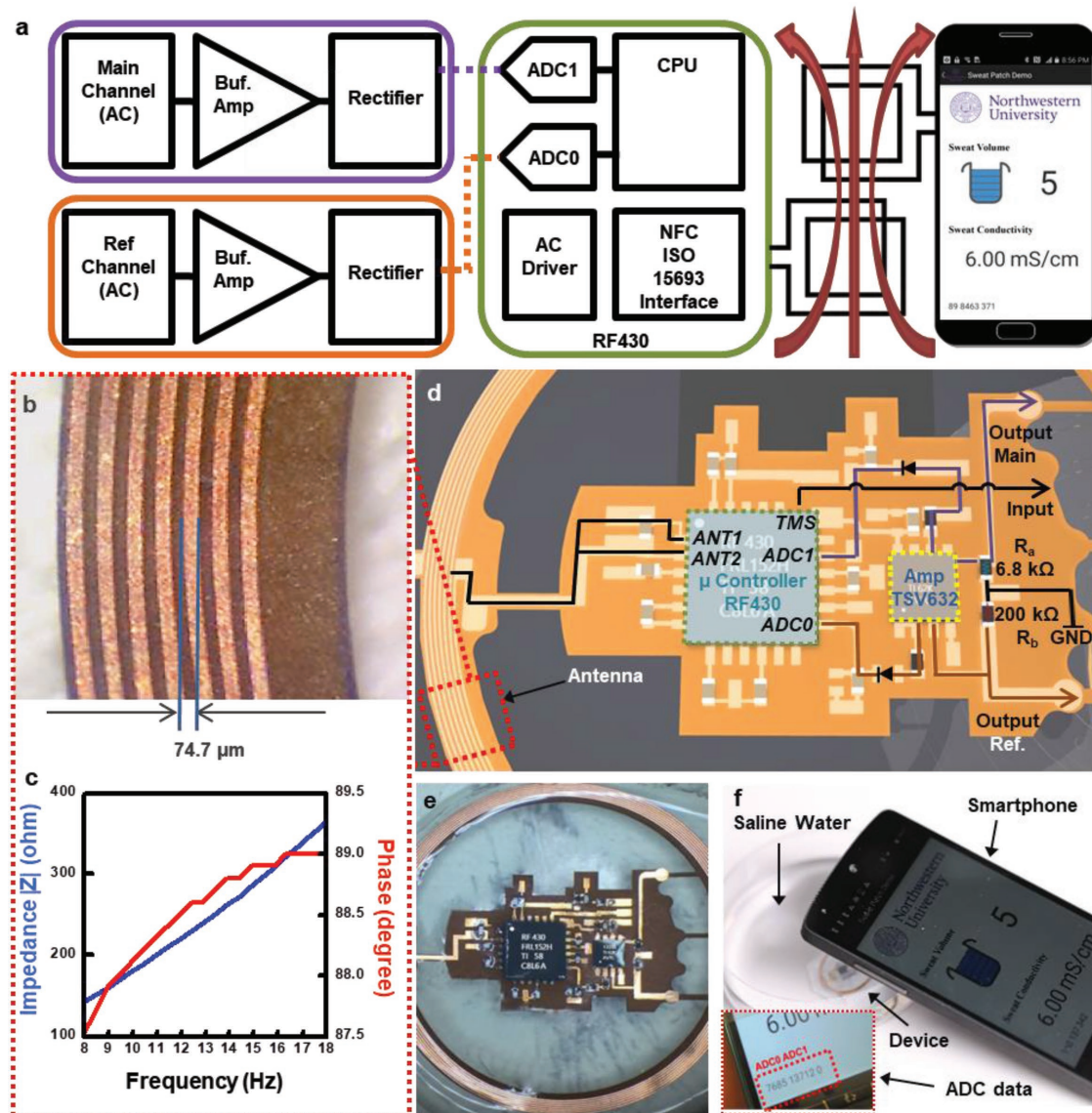
**Figure 2.** Electronics design, measurement strategy, and complete system. a) Schematic diagram of the system and illustration of the electrodes layouts for the main (purple) and reference (orange) microchannel structures, at the device level. b) Schematic illustration of the reference and main electrodes and their interfaces to sweat in the microfluidic system. For the main electrodes, representative resistances for cases where the sweat fills from the inlet to the first (R1), the second (R2), the third (R3), etc. pairs of probing pads are presented. c) Frequency dependent measurements of impedance and phase of artificial sweat in the reference microchannel at various chloride concentrations. d) Measurement of impedance of artificial sweat ( $50 \times 10^{-3}$  M of chloride) in the main microchannel structure. e) Optical images of completed devices, illustrating their flexibility under bending (middle) and twisting (far right).

$$R_n = \alpha \cdot R_r / n \quad (n = 1, 2, 3, 4, \text{ or } 5) \quad (2)$$

where  $\alpha$  is the ratio of the volume of sweat between a pair of probing pads ( $\approx 0.627 \mu\text{L}$ ) and the volume of the reference channel ( $\approx 0.835 \mu\text{L}$ , Figure S2b, Supporting Information). Figure S2c in the Supporting Information presents a schematic circuit of parallel switch resistors in the main channel structure to illustrate the derivation of Equation (2).

Figure S3 in the Supporting Information shows experimental results collected as the flow of artificial sweat ( $\approx 100 \times 10^{-3}$  M chloride concentration; delivered with a syringe pump at a flow rate of  $\approx 4.3 \mu\text{L min}^{-1}$ ) bridges different pairs of probing pads in sequence. The value of ADC1 increases as the total resistance decreases, as expected (measurement frequency before optimization: 13.56 MHz, Figure S3, Supporting Information). The measurement frequency is 5 kHz, selected to minimize any dependence of the phase on electrolyte concentration across a relevant range (chloride between  $25 \times 10^{-3}$  and  $100 \times 10^{-3}$  M, Figure 2c). At this frequency, the impedance varies systematically and significantly across a physiologically relevant range of concentrations when the flow of artificial sweat ( $50 \times 10^{-3}$  M chloride) wets probing pads from 1 to 5, sequentially (Figure 2d).

Figure S4 in the Supporting Information summarizes resistances measured from the reference channel and those calculated with Equation (2) for the case of three human subject tests. These results show that changes in chloride concentration during a typical exercise event are modest and that they do not affect the ability to measure accurately the extent of filling of the measurement channel. For extreme cases where the sweat chloride concentration changes over a wide range, a simple modification to the system can ensure robust operation and readout. Specifically, the optical image and illustration in Figure S5a in the Supporting Information highlights a change that involves insertion of small outline resistors (each  $\approx 5.8 \text{ k}\Omega$ ) along the lengths of the traces for the measurement channel, designed to shift the measured resistances into a favorable range. Figure S5b in the Supporting Information shows the distribution of resistances for two concentrations of chloride ( $5 \times 10^{-3}$  and  $110 \times 10^{-3}$  M) that span the entire physiologically relevant range. In this configuration, the range of resistances associated with each pad, for chloride concentrations between  $5 \times 10^{-3}$  and  $110 \times 10^{-3}$  M, can be used to infer the concentration, without overlap or uncertainty in determinations of the extent of filling.



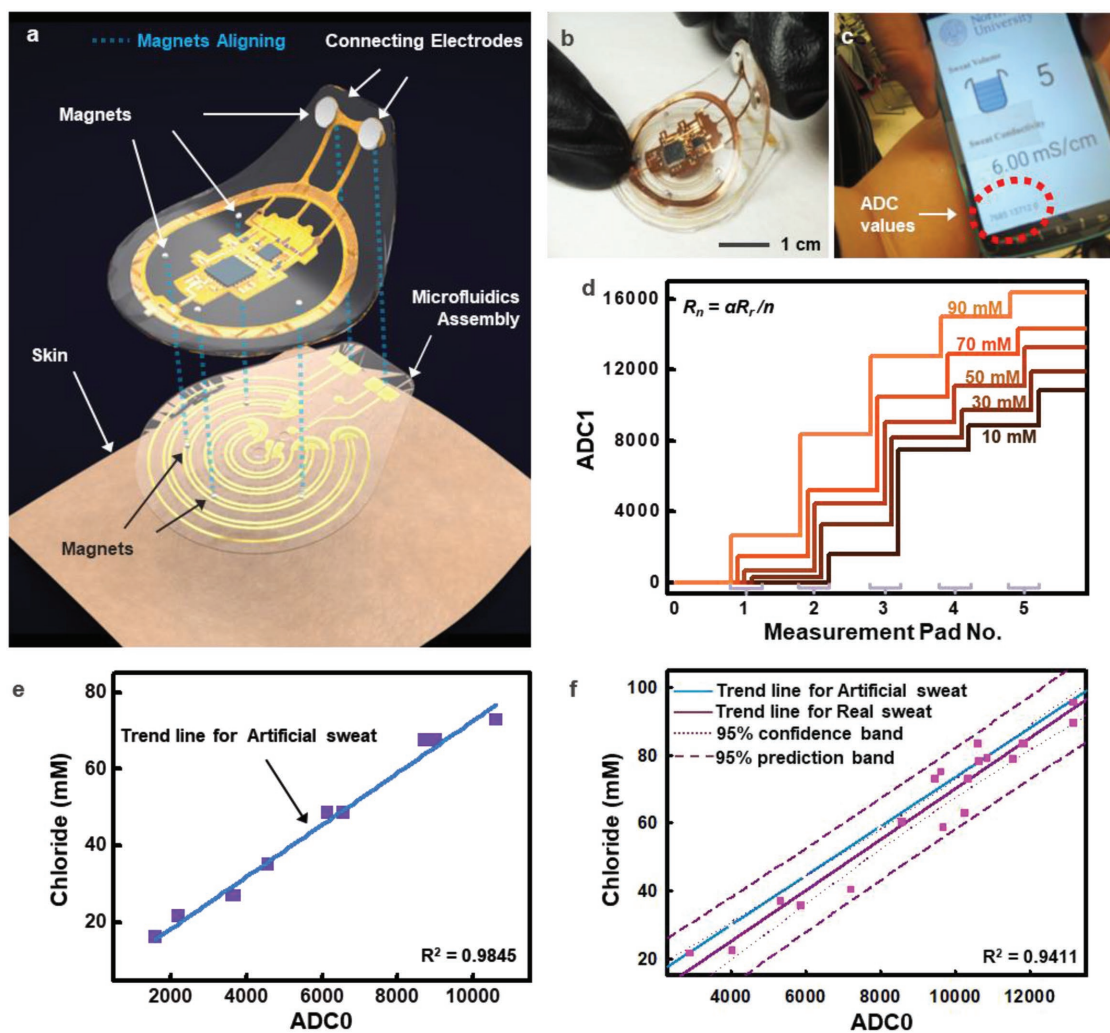
**Figure 3.** Design of the NFC electronics. a) Schematic block diagram of the NFC electronic system and its interface to a sweat microfluidic device and a smartphone. b) Magnified optical image of a portion of the RF antenna. c) Impedance and phase response of the antenna. d) Design of the flexible circuit board with an RF430 microcontroller and a TSV632 amplifier and other components. e) Optical image of a completed electronic system packaged in PDMS and interfaced to a circular antenna. f) Demonstration of operation of the electronics while completely immersed in water via wireless interface to a smartphone.

Figure 2e shows an optical image of a representative device ( $30 \times 36 \text{ mm}^2$ ) during bending and twisting. The soft mechanical construction imposes minimal constraints on natural motions of the skin, and it also minimizes interfacial stresses that could otherwise lead to delamination. The microfluidics layer has a thickness of  $\approx 400 \text{ }\mu\text{m}$ . The electronics module is comparable in thickness with the exception of the NFC die (RF430;  $\approx 1 \text{ mm}$  thickness).

## 2.2. NFC Electronics

An NFC power/communications link provides the energy necessary to drive the electronics in a battery free mode. The

relatively low frequency RF operation (13.56 MHz) allows robust performance in the presence of sweat and biological tissues.<sup>[23,24]</sup> The circuit design in Figure 3a highlights the NFC chip, i.e., RF430, which generates an AC voltage at a frequency defined by general purpose input/output (GPIO) port. A smartphone powers the RF antenna (Figure 3b,c; Q factor of 44.2, Figure S6a, Supporting Information; and inductance of  $2.99 \text{ }\mu\text{H}$ ) to generate AC voltage across the main and reference electrodes channels. These channels share a common node (drive signal  $V_{\text{TMS}}$ ) with pull-down resistors, forming a voltage divider circuit. The divider outputs pass through a buffer (TSV632) to regulate the current and provide measurement isolation, and then a rectifier transforms the signals from AC to DC. The ADCs on the RF430



**Figure 4.** Reversible coupling of the NFC electronic system to the microfluidic platform and quantitative calibration of the measurements. a) Schematic illustration of reversible coupling of the NFC electronic system to the microfluidic platform by use of small-scale, matching magnets, where the blue dotted lines highlight points of alignment. b) Image of the coupling process. c) Visualization of results on the screen of a smartphone via the NFC interface. d) Plot of the effects of chloride concentration on the value of ADC1 for filling up to each of the five pairs of probing pads. e) Plot of chloride concentration for a series of samples of artificial sweat in the reference microchannel and corresponding ADC0 values determined by wireless readout. f) Plot of chloride concentration for a series of samples of human sweat in the reference microchannel and corresponding ADC0 values determined by wireless readout. Laboratory analysis tool (Halide analyzer) enabled to measure accurate concentration of chloride. The purple line corresponds to the calibration determined from analysis of samples of sweat. The other purple dashed lines provide 95% confidence and prediction bands.

acquire data from the reference and main electrode pairs via this circuitry (Figure 3a). The data transmit back to the smartphone through the same RF antenna. The RF range is  $\approx 5$  cm (Figure S6b, Supporting Information) for a transmission coil with areal dimensions of  $40 \times 55$  mm<sup>2</sup>, 4 mm wide metal traces, and four turns. Figure 3d shows the circuit architecture and Figure S7 in the Supporting Information provides detailed information on the individual components and the terminals of the RF430 and TSV632 chips. The resistance values for  $R_a$  and  $R_b$  are chosen to be in the kilohm range (6.8 and 200 k $\Omega$ , respectively) as they are comparable to the resistances of sweat in the microchannel structure. Encapsulation with PDMS protects the electronics from sweat and other external moisture, as shown in Figure S8 in the Supporting Information and Figure 3e. This waterproof design

supports operation with a smartphone while completely immersed in water (Figure 3f).

### 2.3. Reusability and Calibration of the Electronics

Six magnets (two types, with 0.9 and 3 mm diameters; Figure 4a and Figure S9, Supporting Information) guide alignment and physical coupling of the NFC electronics to the microfluidic platform, thereby facilitating removal of the electronics after use. Figure 4b highlights the attachment mechanism, whereby magnetic forces achieve robust mechanical coupling and a reliable, low resistance electrical interface (Figure S9a,b, Supporting Information). Figure S9c–e in the Supporting Information highlights the alignment procedure applied to mount the device on

the skin. Although the impedance and phase response of the inductor capacitor (LC) circuit resonating at 13.56 MHz shifts slightly due to the presence of the magnets (Figure S10, Supporting Information), the overall operation is largely unaffected.

The smartphone serves as a source of RF power to wirelessly activate the NFC electronic sub-system and to wirelessly receive impedance data from the device (Figure 4c). An Android-based software application displays the ADC values. The application first activates the NFC coil of the smartphone to emit pilot electromagnetic pulses. Once the device is in close proximity, the smartphone identifies it as NFC-compatible, sends a command to initiate ADC conversions of the rectified voltages, and prepares for data exchange with an acknowledgement tone. Data received over the NFC link appears on the screen of the smartphone as raw ADC codes (Video S1, Supporting Information).

Measurements using artificial sweat with well-defined chloride concentrations provide means for calibrating the device. Figure 4d summarizes the values of ADC1 for different chloride concentrations and for filling with sweat to different positions along the main channel. The results of Figure 4e correspond to ADC0 values with the reference channel filled with artificial

sweat of different chloride concentrations. Linear regression indicates a high coefficient of determination ( $R^2$ : 0.9845) and a simple relationship between ADC0 and concentration ( $ADC0 = ([\text{Chloride}] - 4.82)/6.7 \times 10^{-3}$ ). The ADC values at various chloride concentrations shown in Figure 4d,e provide information for determining  $R_n$  and  $R_p$ .

Testing with devices mounted on the skin of volunteer subjects (forehead for six subjects, 18 data points obtained from sweat released during exposure in a sauna, during riding of a stationary bike and during running on a treadmill) enables comparison between laboratory analysis (halide analyzer; ion-specific electrodes, ISE, Thermo Scientific "Orin") of the concentration of chloride in human sweat ( $\approx 70 \mu\text{L}$ ) samples extracted from microfluidic devices using a glass syringe (1 mL capacity with 32 gauge needle) and ADC0 values measured directly, as in Figure 4f. The data appear as square symbols. The blue line corresponds to the calibration determined using artificial sweat. The purple dotted line and dashed line are 95% confidence and prediction bands, respectively. These on-body tests demonstrate that the NFC system provides reliable data, in situ, with excellent correspondence to actual values.

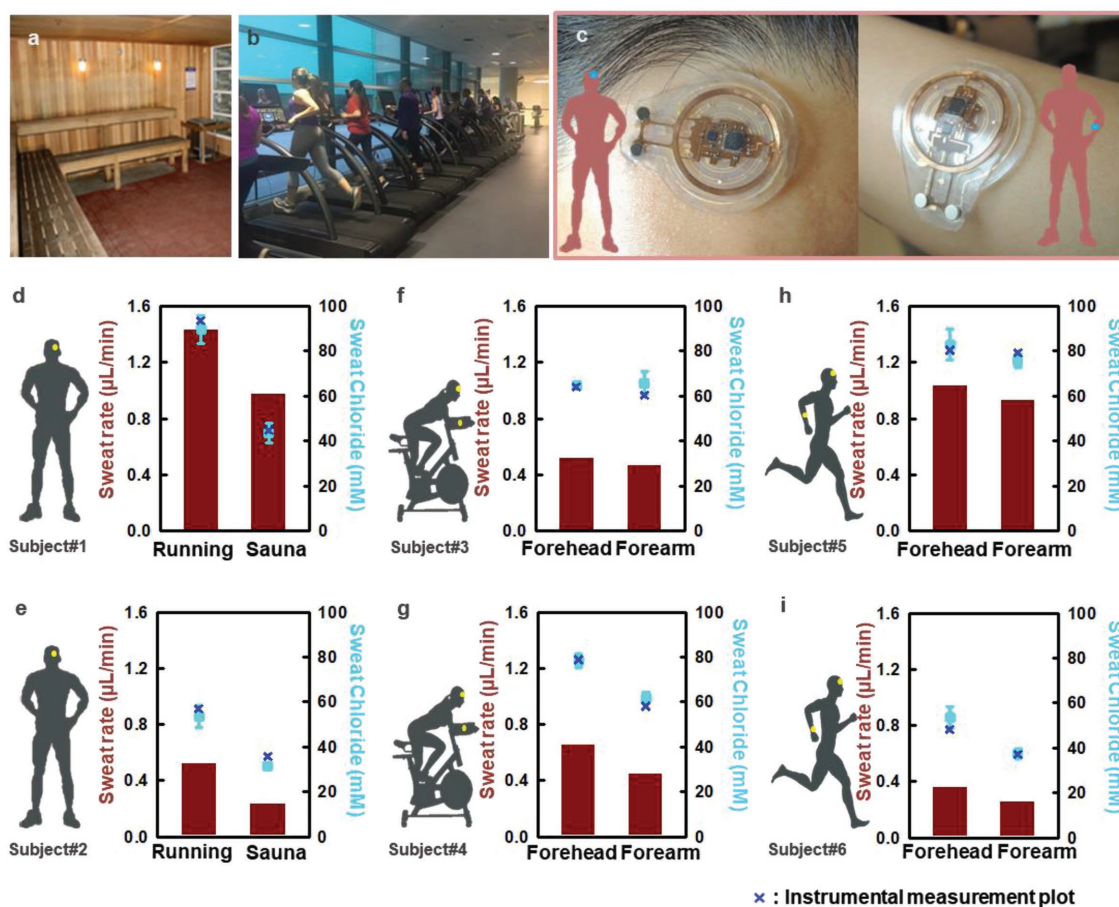


**Figure 5.** On-body human testing. a) Sauna environment for inducing sweat without physical exercise. b) Gym environment for inducing sweat by physical exercise. c) Pictures of devices deployed on the forehead and forearm. d,e) Sweat rate and chloride concentration measured from subjects #1 and #2 during exercise (running on a treadmill) and exposure to a sauna. f,g) Sweat rate and chloride concentration for different regions of the body on subjects #3 and #4 during exercise (riding on a stationary bike). h,i) Sweat rate and chloride concentration for different regions of the body on subjects #5 and #6 during exercise (running on a treadmill).

## 2.4. On-Body Testing in Nonlaboratory Settings

Additional on-body tests involve six volunteers with sweating induced by heat/humidity or by physical exercise. Studies to compare sweating in heat and exercise conditions involve two subjects (#1 and #2) with devices mounted on the forehead, while at rest in a sauna for 19–28 min (Figure 5a; temperature and humidity 70–80 °C and ≈20%, respectively) and running on a treadmill for 17–29 min (four levels of incline at speeds of 8–10 km h<sup>-1</sup>) in a gym environment (Figure 5b; temperature and humidity ≈25 °C and ≈60%, respectively). Regional sweat rate comparisons involve four remaining subjects with devices mounted on the forehead and the forearms (Figure 5c), two of whom (subjects #3 and #4) on stationary bikes (20–29 min vigorously pedaling at medium difficulty levels) and the other two (subjects #5 and #6) on treadmills (17–26.5 min, four levels of incline at speeds of 8–10 km h<sup>-1</sup>).

Wirelessly collected values of ADC0 determine the electrolyte concentration via the calibration results in Figure 4f. Data from ADC1 define the position of the filling front, to within the spacing between adjacent probing pads, as sweat moves through the main microchannel. With the dimensions of the channel, these results yield the local volume of collected sweat. Temporal information captured from the smartphone during a pair of wireless readings yields the sweat rate. Figure 5d,e shows the results for subjects #1 and #2. In both cases, exercise induces higher rates of sweating than sauna exposure, and the chloride concentrations are proportional to sweat rate. These trends are similar to those published previously using other approaches.<sup>[25–28]</sup> Figure 5f–i compares regional sweating on four subjects. The results observed in Figure 5f,g for operating a stationary bike and Figure 5h,i for running on a treadmill indicates that the rate of sweating from the forehead is higher than that from the forearm, consistent with previous reports.<sup>[29,30]</sup> The wireless interface provides a convenient measurement modality (Video S1, Supporting Information). Figure S11 in the Supporting Information summarizes human subject tests of the sweat loss measured using these devices and using conventional absorbent pads. The results exhibit good, quantitative agreement.

## 3. Conclusion

The soft microfluidic and flexible electronic technologies presented in this study yield a simple, wireless, and battery-free digital platform for monitoring sweat rate, total sweat loss, and electrolyte concentration in real time. The key differentiating features of this platform are in reusable flexible electronics modules, which exploit NFC wireless communication and energy harvesting protocols, and integration strategies with skin-compatible microfluidic systems designed for precise storage and capture of microliter volumes of sweat released from eccrine glands. Benchtop studies of the microfluidic and electronic subsystems define the basic operating principles. Field studies on human subjects further demonstrate the practical feasibility of in situ data collection during rest and vigorous exercise, in strong agreement with ex situ approaches using benchtop diagnostic instruments. The skin-compatible designs and ability to quantify sweat volume and sweat electrolytes in real-time have important implications for health

monitoring, sports performance tracking, and nutrition management in uncontrolled settings.

## 4. Experimental Section

**Fabrication of the Measurement Electrodes Platforms:** Spin casting of PI (spin coated at 3000 rpm for 30 s and baked at 110 °C for 10 min) defined a layer of 1.5 μm thickness on a sheet of Cu clad with a thin film of Cu (3 μm/18 μm thickness, DuPont, Wilmington, DE). Removal of the Cu sheet allowed the PI-Cu to be laminated, with PI side down, onto a glass slide (Fisherbrand, Pittsburgh) coated with polydimethylsiloxane (PDMS; Sylgard 184, Dow Corning, Midland, MI; mixed at a 10:1 ratio of base to curing agent by weight). Deposition of Au onto the Cu by electron-beam evaporation (400 Å, Temescal, Livermore, CA) yielded a chemically inert measurement interface to the sweat. Photolithography (photoresist AZ 4620; spin casting at 3000 rpm for 30 s, baking on a hot plate at 110 °C for 3 min, UV irradiance for 300 mJ cm<sup>-2</sup> and development for ≈40 s with developer AZ 400 K/deionized water solution of 1:2 volume ratio), wet etching (HFCE100 copper etchant, Transense, Oxfordshire, UK; ≈2 min with frequent rinsing by water), and oxygen plasma etching (200 mtorr, 20 sccm O<sub>2</sub>, 200 W power for 30 min) patterned the Au–Cu–PI layers into the desired electrodes geometries. Transferring the resulting structure onto a water-soluble tape allowed electron-beam deposition of Ti and SiO<sub>2</sub> (100 Å and 300 Å, respectively) onto the backside of the PI. Bonding between the electrodes and the PDMS occurred via physical contact after exposing the SiO<sub>2</sub> side of electrodes platform and the PDMS to O<sub>2</sub> plasma (Harrick Plasma Oxygen Cleaner, Ithaca, NY) at 18 W RF power.

**Soft Lithographic Fabrication of the Microfluidic Systems:** Soft lithographic procedures formed thin slabs of PDMS (Sylgard 184, 20:1, spin cast at 250 rpm and cured in an oven at 70 °C for 4 h) with features of surface relief defined by those of a silicon mold. Fabrication of the mold began with photolithography (photoresist, KMPR1010, spin casting at 3000 rpm for 30 s, baking on a hot plate at 110 °C for 3 min, UV irradiance for 300 mJ cm<sup>-2</sup>, and development for 2 min with developer MF917) deep reactive-ion etching (STS Pegasus inductively coupled plasma-deep reactive ion etching (ICP-DRIE), SPTS Technologies Ltd, UK) of a silicon wafer to a depth of 200 μm. Bonding of the PDMS/electrodes substrate against this PDMS microfluidics layer after wetting the raised regions with a small amount uncured PDMS enabled precision alignment, assembly and bonding (10:1 baking on a hot plate 70 °C for 30 min).

**Electronics Assembly and Data Visualization:** Fabrication began with patterning of a two-layer printed circuit board by processing of multilayer foils of Cu–PI–Cu (18 μm/75 μm/18 μm) with a professional-grade laser cutter (U4; LPKF Laser, Germany). The main processor, RF430FRL152HCRGER (RF430, ISO/IEC 15693, ISO/IEC 18000-3; Texas Instruments, Dallas, TX where ISO/IEC is a joint technical committee of the International Organization for Standardization and the International Electrotechnical Commission) served as the NFC platform, with the ability to rectify incident power from a smartphone device up to 720 μW at 2.0 V, depending on coupling efficiency, and relaying data over the 13.56 MHz communications link. The RF430 supported 14-bit Sigma-Delta ADC with triple analog inputs at an input range up to 900 mV and maximum sampling frequency of 2 kHz, down-sampled to 1 Hz resolution. Signal amplification and measurement of the main and reference channels used another chip, TSV632IQ2T (STMircocoelectronics, Geneva, Switzerland), as dual-channel operation amplifiers with low energy consumption (60 μA at 5 V) and large unity gain-bandwidth (800 kHz). On power-up, the system sourced a 5 kHz, rail-to-rail square wave to the channels, causing an AC current to flow through the collected sweat. The magnitude of this current is proportional to the concentration of ions in the sweat, as an electrical impedance that caused the sourced 5 kHz waveform to attenuate during passage through the sweat. This attenuation reduced the amplitude of the waveform whose rectified voltage was buffered and measured by the TSV632 and ADC, respectively. This rectified voltage level was sampled,

processed, and relayed to an NFC compatible reader by the RF430. An NFC-compatible smartphone (LG Nexus 5X; LG, Seoul, South Korea) and custom-developed application for the Android operating system enabled visualization of the data.

**Device Packaging:** The molded PDMS substrate, as shown in Figure S8a in the Supporting Information, served as the platform for NFC electronics integration and packaging. Placing the electronics and mechanical coupling magnets (0.9 mm diameter) on the PDMS and the applying and curing an overcoat of PDMS as shown in Figure S8b,c in the Supporting Information yielded a waterproof covering. Additional magnets (3 mm diameter) placed on the electronics and the microfluidics as shown in Figure S8b in the Supporting Information provided mechanical and electrical coupling.

**Human Tests:** On-body tests with six healthy volunteers involved sweating induced by riding on a stationary bike, running on a treadmill or sitting in a sauna. Each subject gave full, informed signed consent before participating in on-body experiments. The sauna provided an environment with ≈20% humidity at temperatures between 70 and 80 °C. Subjects wore sportswear such as shorts and t-shirts for the test. The environment for exercise induced sweating had a humidity of ≈60% and temperature of ≈25 °C. Prior to mounting the devices, the skin was cleaned by rubbing with 70% ethanol. Recovery of sweat samples from the devices relied on a glass syringe (1 mL capacity with 32 gauge needle). A halide analyzer measured the chloride concentration, using an ISE (Thermo Scientific “Orin”) calibrated to the  $1 \times 10^{-3}$ – $100 \times 10^{-3}$  M level.

## Supporting Information

Supporting Information is available from the Wiley Online Library or from the author.

## Acknowledgements

S.B.K., K.L., and M.S.R. contributed equally to this work. J.K. acknowledges the Research Program of National Research Foundation of Korea (NRF) funded by Korean government (MSIT) (NRF-2018R1C1B5045524 and NRF-2017M3A9F1031270).

## Conflict of Interest

The authors declare no conflict of interest.

## Keywords

flexible electrodes, microfluidics, near field communication, sweat conductivity

Received: July 23, 2018  
Revised: September 12, 2018  
Published online: October 9, 2018

- [1] R. Ruddy, R. Anolik, T. F. Scanlin, *Clin. Pediatr.* **1982**, 21, 367.
- [2] P. M. Gopinathan, G. Pichan, V. M. Sharma, *Arch. Environ. Health: Int. J.* **1988**, 43, 15.
- [3] M. A. Baker, *J. Physiol.* **1989**, 417, 421.
- [4] K. Holte, H. Kehlet, *Acta Anaesthesiol. Scand.* **2002**, 46, 1089.
- [5] N. P. Walsh, S. J. Laing, S. J. Oliver, J. C. Montague, R. Waters, J. L. J. Bilzon, *Med. Sci. Sports Exercise* **2004**, 36, 1535.
- [6] K. Ohara, *Jpn. J. Physiol.* **1966**, 16, 274.
- [7] S. M. Fortney, C. B. Wenger, J. R. Bove, E. R. Nadel, *J. Appl. Physiol.: Respir., Environ. Exercise Physiol.* **1984**, 57, 1688.
- [8] N. J. Caplen, E. W. F. W. Alton, P. G. Middleton, J. R. Dorin, B. J. Stevenson, X. Gao, S. R. Durham, P. K. Jeffery, M. E. Hodson, C. Coutelle, L. Huang, D. J. Porteous, R. Williamson, D. M. Geddes, *Nat. Med.* **1995**, 1, 39.
- [9] R. C. Boucher, *Annu. Rev. Med.* **2007**, 58, 157.
- [10] J. C. Davies, E. W. F. W. Alton, A. Bush, *Clin. Rev.* **2017**, 335, 1255.
- [11] H. M. Emrich, E. Stoll, B. Friolet, J. P. Colombo, R. Richterich, E. Rossi, *Pediatr. Res.* **1968**, 2, 464.
- [12] J. L. Lezana, M. H. Vargas, J. Karam-Bechara, R. S. Aldana, M. E. Furuya, *J. Cystic Fibrosis* **2003**, 2, 1.
- [13] W. Gao, S. Emaminejad, H. Y. Y. Nyein, S. Challa, K. Chen, A. Peck, H. M. Fahad, H. Ota, H. Shiraki, D. Kiriya, D. Lien, G. A. Brooks, *Nature* **2016**, 529, 509.
- [14] H. Y. Y. Nyein, W. Gao, Z. Shahpa, S. Emaminejad, S. Challa, K. Chen, H. M. Fahad, L. Tai, H. Ota, R. W. Davis, *ACS Nano* **2016**, 10, 7216.
- [15] A. Koh, D. Kang, Y. Xue, S. Lee, R. M. Pielak, J. Kim, T. Hwang, S. Min, A. Banks, P. Bastien, M. C. Manco, L. Wang, K. R. Ammann, K.-I. Jang, P. Won, S. Han, R. Ghaffari, U. Paik, M. J. Slepain, G. Balooch, Y. Huang, J. A. Rogers, *Sci. Transl. Med.* **2016**, 8, 366ra165.
- [16] A. J. Bandodkar, J. Wang, *Cell Press* **2016**, 32, 363.
- [17] J. Heinkenfeld, *Electroanalysis* **2016**, 28, 1242.
- [18] J. Choi, R. Ghaffari, L. B. Baker, J. A. Rogers, *Sci. Adv.* **2018**, 4, eaar3921.
- [19] S. B. Kim, Y. Zhang, S. M. Won, A. J. Bandodkar, Y. Sekine, Y. Xue, J. Koo, S. W. Harshman, J. A. Martin, J. M. Park, T. R. Ray, K. E. Crawford, K. T. Lee, J. Choi, R. L. Pitsch, C. C. Grigsby, A. D. Strang, Y. Y. Chen, S. Xu, J. Kim, A. Koh, J. S. Ha, Y. Huang, S. W. Kim, J. A. Rogers, *Small* **2018**, 14, 1703334.
- [20] D. C. Grahame, B. A. Soderberg, *J. Chem. Phys.* **1954**, 22, 449.
- [21] Z. Osman, M. I. Mohd Ghazali, L. Othman, K. B. Md Isa, *Results Phys.* **2012**, 2, 1.
- [22] Q. Yuan, K. Yang, J. Wu, *Microfluid. Nanofluid.* **2014**, 16, 167.
- [23] R. Want, *IEEE Pervasive Comput.* **2011**, 10, 4.
- [24] R. Feynman, *The Feynman Lectures on Physics*, 2nd ed., Addison-Wesley, Reading, MA, USA **2005**.
- [25] T. Fukumoto, T. Tanaka, H. Fujioka, S. Yoshihara, T. Ochi, A. Kuroiwa, *Clin. Cardiol.* **1988**, 11, 707.
- [26] L. J. McCutcheon, R. J. Geor, M. Jessie Hare, G. L. Ecker, M. I. Lindinger, *Equine Vet. J.* **1995**, 20, 153.
- [27] D. B. Dill, F. G. Hall, W. Van Beaumont, *J. Appl. Physiol.* **1966**, 21, 99.
- [28] L. B. Baker, *Sports Med.* **2017**, 47, 111.
- [29] J. Smith, G. Havenith, *Eur. J. Appl. Physiol.* **2011**, 111, 1391.
- [30] N. A. Taylor, C. A. Machado-Moreira, *Extreme Physiol. Med.* **2013**, 2, 4.